2026 IEEE International Conference on Robotics and Automation (ICRA 2026)
June 1-5, 2026. Vienna, Austria

Near-Field Driven Origami-Based Bio-Inspired Jellyfish Robot

Sen Wang, Chengxiang Lu, Lepeng Chen, Yi Tang, Mansen Chen, Shuai Zhang, and Jun Liu*

Abstract— **The development of bio-inspired jellyfish robots holds significant benefits for autonomous aquatic systems due to jellyfish's efficient water jet propulsion. However, the current design of jellyfish robots still faces challenges in balancing high biological fidelity with the demands of lightweight, compact design and high-speed locomotion. This study presents a bio-inspired jellyfish robot that emulates the shape and efficient water jet propulsion of natural jellyfish. The origami-based bell and supporting structure are designed to form an efficient water-jet cavity. As the primary components of the robot, they endow the robot with the ability to self-recover to a stable state during locomotion, thereby reducing energy consumption. Additionally, they replace traditional transmission mechanisms, thereby reducing the weight and complexity of the robot. An optimization model is established to determine the optimal parameters of the jellyfish robot. Furthermore, a near-field magnetic actuation system is designed to drive the robot, enabling contactless and silent underwater driving without waterproofing requirements. The robot features a diameter of 101.6 mm, a height of 63.8 mm, and a weight of 12.5 g. Experimental results demonstrate a maximum locomotion speed of up to 96.2 mm/s.**

I. Introduction

Underwater robots, as an essential tool for the exploration and exploitation of marine resources, have demonstrated significant potential in fields such as seabed exploration, aquatic environment monitoring, and subsea operations [1]. Among numerous marine organisms, jellyfish are considered one of the best choices for biomimetic underwater robot design due to their distinctive axial-symmetrical, streamlined morphology and highly efficient water jet propulsion motion mode. Consequently, bio-inspired underwater robots based on jellyfish have been extensively studied and developed within the research community [2], [3].

Existing bio-inspired jellyfish robot designs typically employ traditional and stable actuation methods such as electric motors and pneumatics, or utilize novel smart materials like shape memory alloy (SMA), dielectric elastomer actuators (DEA), and hydraulically amplified self-healing electrostatic (HASEL) actuators. Electric motor-driven systems generally require the design of rigid transmission mechanisms, such as linkages and gear trains, which increase the overall weight and complexity of the robot. Additionally, internal friction within these mechanisms will cause energy losses during operation [4], [5]. Pneumatic jellyfish robots possess soft and bio-inspired morphologies; however, they require the design of air channels, which complicates fabrication, and the inflation and deflation processes limit their actuation frequency [6], [7]. SMAs facilitate miniaturization and lightweight design, but their reliance on Joule heating results in relatively slow response speeds [8], [9]. DEA and HASEL can better mimic the soft muscle movements of jellyfish, however, they typically operate at high voltages, often capable of reaching several kilovolts, which poses application challenges [10]–[12]. Therefore, balancing lightweight, compact design with high-efficiency actuation remains a significant challenge.

Near-field magnetic actuation is a method that utilizes magnetic forces between different electromagnetic coils or between electromagnetic coils and magnets to achieve actuation. The dimensions of the coils and magnets can be designed according to the required magnetic force for specific applications. In close-distance driving scenarios, this approach enables faster response and more precise position control in a contactless manner [13]. In addition to applications in large-scale biomimetic robot design [14], this technique allows for the development of robots that are small-scale, lightweight, and compact [15]. Additionally, unlike jellyfish robots that rely on external magnetic field-driven methods [16], this approach eliminates the need for large external equipment and reduces dependence on environmental conditions, thereby significantly enhancing the robot's autonomous locomotion capabilities. It is particularly well-suited for the design of bio-inspired jellyfish robots.

Origami technology facilitates the creation of three-dimensional structures using planar manufacturing methods, allowing for lightweight designs with programmable motions such as unfolding and folding. This approach has been widely applied in various engineering fields [17]–[19]. Notably, origami structures with stable-state characteristics, such as Waterbomb-based origami, can maintain a stable configuration in the non-actuated state due to their inherent self-recovery ability [20], [21]. These features make them suitable for applications that require reliable self-recovery performance [22]. Such insights provide valuable inspiration for the design of bio-inspired jellyfish robots: by integrating origami structures with stable-state properties, the robots can achieve contraction and expansion movements while self-recovering to a stable position during their motion cycle, thereby improving the driving efficiency.

Therefore, to achieve high-speed movement based on water jet propulsion inspired by jellyfish, while also fulfilling the requirements for a biomimetic, small-scale, and lightweight design, we design the origami-based bell and origami-based supporting structure with stable state properties as the core components of the robot. These two origami structures, once assembled, form a cavity that effectively mimics the water jet propulsion movement of jellyfish. Since

This work was supported by the Research Grants Council of Hong Kong under Grant Nos. 11217922, 11212321, and 21212720. *(Sen Wang, Chengxiang Lu, and Lepeng Chen contributed equally to this work.) (Corresponding author: Jun Liu.)*

Sen Wang, Chengxiang Lu, Lepeng Chen, Yi Tang, Mansen Chen, Shuai Zhang, and Jun Liu are with the Department of Data and Systems Engineering, The University of Hong Kong, Hong Kong, China (e-mails: senwang@hku.hk; chengxiang.lu@connect.hku.hk; lepechen@cityu.edu.hk; yiitang@hku.hk; manschen@hku.hk; zhangstz@hku.hk; dr.jun.liu@hku.hk).

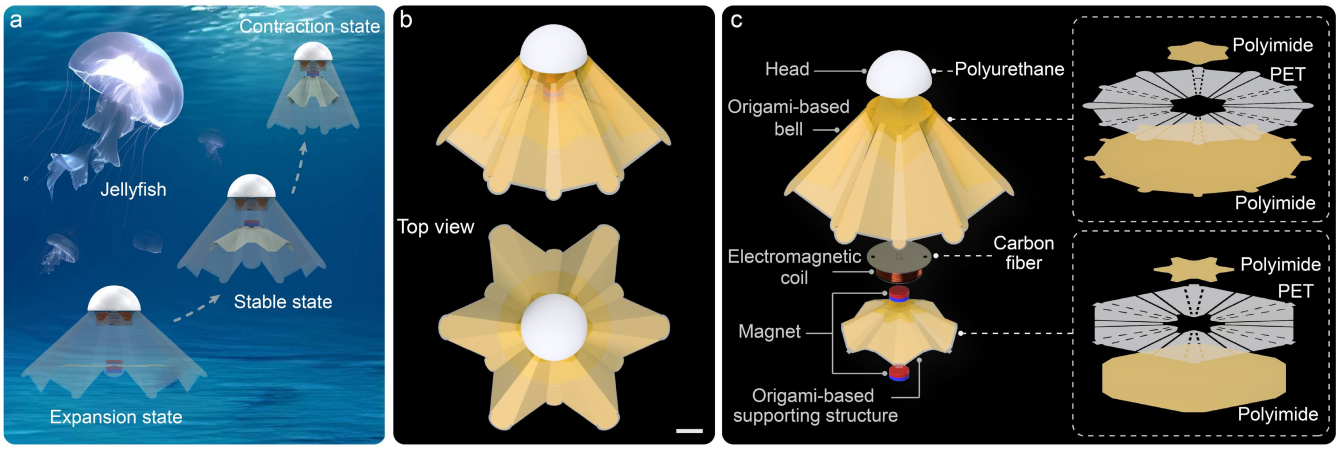

Fig. 1. Structure overview and fabrication of bio-inspired jellyfish robot. (a) Concept diagram and the three states of bio-inspired jellyfish robot. (b) The overview structure of the designed robot. (c) The composition and fabrication of bio-inpired jellyfish robot. Scale bar, 10 mm.

the origami-based supporting structure pushes water in the form of the entire surface during movement, it can generate a larger water displacement, thereby significantly improving the robot's locomotion speed. To realize efficient transmission, a near-field magnetic actuation system is developed. By driving the magnet's movement with electromagnetic coils, the magnetic force can be directly applied to the origami mechanism via the magnet. This approach replaces traditional rigid transmission mechanisms, significantly reducing system complexity and weight, while also minimizing energy loss due to friction within the transmission process. Additionally, this actuation method enables silent motion directly in water without the need for waterproofing measures. Moreover, the combination of the two origami structures imparts stable state characteristics to the robot, enabling it to be powered solely during the contraction phase for water displacement. During the expansion phase, the robot can rely on its elastic force to return to the stable state, thereby achieving energy-efficient operation. Apart from the buoyancy block at the head, the robot contains only a near-field magnetic actuation system and two origami-based structures. Therefore, a bio-inspired jellyfish robot with a small-scale, lightweight, and compact design can be realized.

The remainder of this paper is organized as follows: Section II details the design of the origami-based structures, actuation system, and bio-inspired jellyfish robot. Section III tests and analyzes the locomotion performance of the robot. Section IV summarizes this research.

II. Bio-Inspired Design and Analysis

A. Overall Bionic Structure Design and Fabrication

To emulate the efficient pulsatile locomotion of natural jellyfish, this study proposes an origami-based bio-inspired jellyfish robot using near-field magnetic actuation. The locomotion of natural jellyfish can be generally divided into three stages: the relaxation stage, during which the bell adopts an expanded, hemispherical shape with water filling the body, allowing for free drifting; the expansion stage, where the bell actively opens upward, increasing in volume and drawing in more water; and the propulsion stage, in which the muscles rapidly contract to compress the bell, expelling water and generating upward thrust. Through this repetitive contraction and relaxation of the bell, jellyfish generate a continuous, water jet propulsion motion. Inspired by this locomotion, as illustrated in Fig. 1(a), the origami-based bio-inspired jellyfish robot achieves three states, i.e., expansion, stable, and contraction states. The contraction motion is driven by a near-field magnetic actuation system. While the expansion motion relies on the inherent stability of the origami structures to enable the robot's automatic recovery.

The robot is composed of three main components: a lightweight head, a near-field magnetic actuation system, and two origami-based structures (Fig. 1(b) and (c)). For the origami-based structure, the outer one is origami-based bell, while the inner one named origami-based supporting structure. The fabrication process of the designed bio-inspired jellyfish robot is simplicity and efficiency. Firstly, the origami-based bell and supporting structure can be rapidly fabricated in a planar form. They both consist of two layers of polyimide (PI) tape and an intermediate layer of polyethylene terephthalate (PET) sheet (Fig. 1(c)). The 0.15 mm thick PET is cut into the designed shape using Cricut Maker 4; then, the two 0.1 mm thick PI tapes are attached on the intermediate PET sheet. PET determine the shape of structure and provides stiffness, while PI tapes define foldable flexible hinges. By folding along dashed and radial cut lines to form the three-dimensional origami structure at the stable state. For actuation, the electromagnetic coil is wound from 0.3 mm copper wire around a carbon fiber frame (fabricated from laser-cut carbon fiber sheets and tube) with robustness. The two N52 permanent magnets can effectively attach the origami structure in the middle through their magnetic attraction, enabling coaxial assembly without the need for bonding. During locomotion, the permanent magnets can directly transmit the driving force to the origami-based supporting structure. Furthermore, origami-based bell is bonded to the carbon fiber frame, while the two origami structures are positioned relative to each other using a mortise and tenon connection method and secured with PI tape at the connect position to form a cavity. Finally, a polyurethane head is fabricated and attached at the top of origami-based bell to provide buoyancy and stabilize the robot during locomotion.

B. Origami-Based Structures Design and Analysis

In this design, the three-dimensional cavity formed by origami-based bell and supporting structure are designed for providing propulsion when locomotion, achieving a dual

biomimetic effect in both form and function. To increase the thrust generated during cavity contraction, the inner origami-based supporting structure should maximize the contact area with water during movement, thereby increasing the water displacement per driven cycle. Therefore, based on the split-fold waterbomb base [20], an improved waterbomb-based origami design method is proposed to design the origami-based bell and supporting structure, as shown in Fig. 2(a). These two structures both exhibit bistable characteristic, but this paper only uses and discusses the single stable state performance in the upper horizontal position.

To design origami-based supporting structure, a regular polygonal pattern should be constructed, where the number of edges can be arbitrary. Taking a regular hexagonal pattern (the number of valley facets $n_v = 6$) as an example as shown in (i) of Fig. 2(a), the process begins by identifying the intersection of the diagonals as the center point *O*. A line connecting this center to a vertex of the regular polygon is used as symmetry axis. And two valley creases intersecting at the center point are then arranged and with an angle θ_v between them. Two valley creases and the polygon edges will intersect at two points, the edge connecting these two points is named as installation edge and the length is L_e. The distance from this edge to center point is R_s. Circular arraying these two valley creases around center point at all six vertices of the hexagon, six valley facets are formed (pink facets). Subsequently, connecting the adjacent installation edges and removing the excess area of pattern yields the initial origami shape. Then, arrange six pairs of mountain creases with angle θ_m at the centerline position, obtaining six mountain facets (blue facets), in this design, $\theta_v = \theta_m$. Finally, cut the central grey area (diameter is D_m) for magnet installation, and the origami-based supporting structure can be obtained.

Then, for the parameters of origami-based bell ((ii) in Fig. 2(a)), the number of valley facets is equal to n_v. The target diameter D_t should be designed at first since it determines the connecting position of the origami-based supporting structure and bell. Then, to prevent interference during movement, the widths of the valley facets at the connection positions are equal to L_e. Furthermore, the angle $\theta_{bv} = 2\left(\arctan\left(L_e / D_t\right)\right)$, while $\theta_{bm} = \theta_m$. By increasing the scale of the bell to a radius of R_b, an additional ring-shaped structure resembling skirt can be obtained to provide additional thrust during swinging. The ring area between two circles of diameters D_t and D_b representing its scale. Finally, according to the size of head D_h and cut the central installation area (grey area), the origami-based bell can be designed and further fabricated.

For origami-based supporting structure, after folding along the creases into a three-dimensional shape, its center will protrude to form a stable state. Pressing the protruded center can cause it to move downward to a horizontal position, with a distance of d_s, while the upward reaction forces F_u will be generated by the structure. The control variable experiment was conducted to analyze the effects of parameters θ_v, n_v, and R_s on F_u and d_s. The three parameters were set to values $[5°, 10°, 15°]$, $[4, 6, 8]$, and $[20, 30, 40]$, respectively. The three conclusions which can offer valuable insights and references for this type of origami applications across different fields are as follow:

a) When the number of valley facets n_v and radius R_s are the same, both upward reaction force F_u and movable distance d_s of the structure decrease with increasing angle θ_v ((i) in Fig. 2(b)).

b) When angle θ_v and radius R_s are the same, the upward reaction force F_u increase with increasing the number of valley facets n_v, but movable distance d_s decrease with increasing n_v ((ii) in Fig. 2(b)).

c) When the number of valley facets n_v and angle θ_v are the same, both upward reaction force F_u and movable distance d_s of the structure increase with increasing radius R_s ((iii) in Fig. 2(b)).

C. Parameter Optimization of Bio-Inspired Jellyfish Robot

Since the cavity between the two origami-based structures exhibits rotational symmetry, the motion is also identical at each symmetric position. When the supporting origami structure moves upward, water is evenly expelled from the gap between the two structures, and the water expulsion occurs at symmetrical locations, as shown in Fig. 2(c). Therefore, the motion of robot can be simplified as the movement of a four-bar linkage mechanism, the two origami-based structures are respectively equivalent to the linkages A_0C_0 and BC_0. And the magnet can be equivalent to a slider. For the origami-based supporting structure, the horizontal position and the full-distance position are the two limit positions. The distance between these two positions is denoted as d_t. When the supporting structure achieves a full distance motion, it can transition from A_0C_0 to A_1C_1, which in turn drives the bell from BC_0 to BC_1. And a swing angle δ between BC_0 and BC_1 will be obtained. Analysis indicates that, for this robot, a larger swing angle leads to increased water displacement in the cavity during a full distance motion. Additionally, a larger swing of the bell will also facilitate the robot's swimming, similar to the paddling motion of a fish tail. Therefore, maximizing the swing angle can be used as the optimization objective to determine the size of origami-based structures.

As shown in Fig. 2(c), the length of equivalent linkages A_0C_0 and BC_0 are defined as L_1 and L_2, respectively, with $L_1 = R_s - D_m / 2$ and $L_2 = \left(D_t - D_h\right) / 2$. And the three edge lengths of triangle $\triangle A_1BD$ are *a*, *b*, and *c*, respectively. At the initial position, angle θ_1 can be obtained as

$$\theta_1 = \arcsin\left(\frac{L_1 - a}{L_2}\right). \tag{1}$$

At the final position, to obtain the angle θ_2, it is necessary to first determine the following parameters:

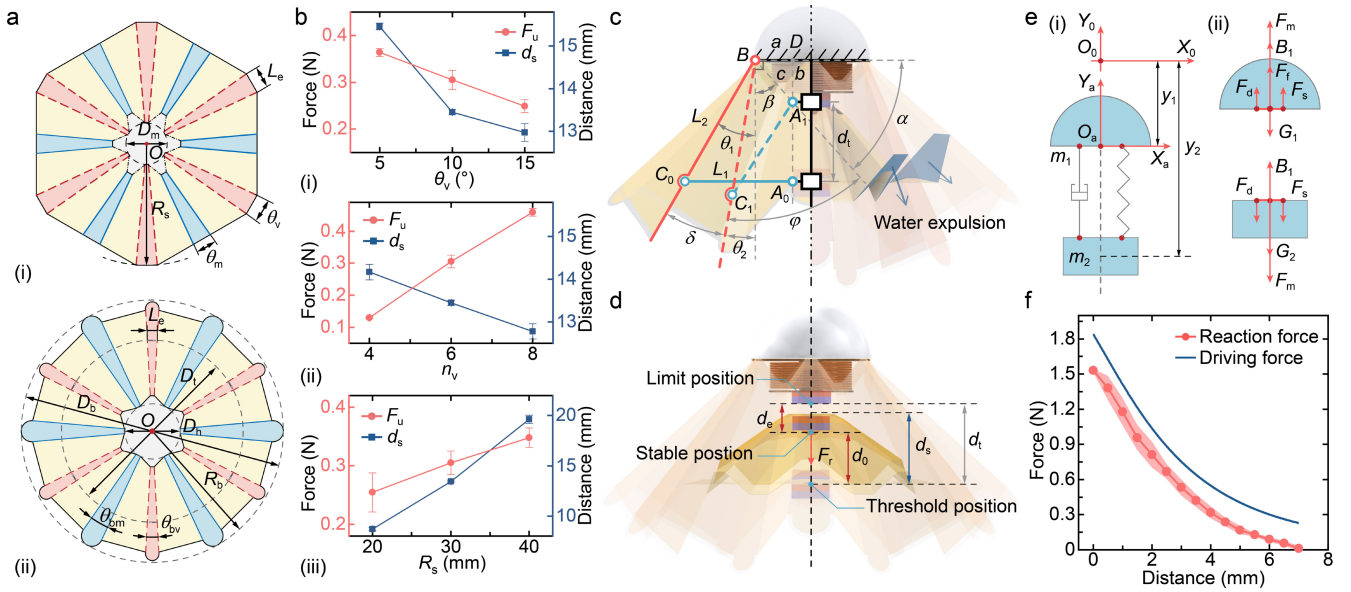

Fig. 2. Structure design and analysis of bio-inspired jellyfish robot. (a) Structure design of origami-based supporting structure (i) and bell (ii). (b) The reaction force F_u and moveable distance d_s with different angles θ_v, the number of valley facets n_v, and designed radii R_s of origami-based supporting structure, respectively. (c) Optimization model development to obtain the maximum swing angle of the origami-based bell. (d) The configuration of the robot after installing the two origami-based structures. (e) Establishment of the dynamic model. (f) The driving force generated by near-field magnetic actuation system is designed to match the reaction force F_r of robot's structure.

$$\begin{cases} c = \sqrt{a^2 + b^2} \\ \alpha = \arcsin\left(\dfrac{b}{c}\right) \\ \beta = \dfrac{\pi}{2} - \alpha \\ \varphi = \arccos\left(\dfrac{L_2^2 + c^2 - L_1^2}{2L_2 c}\right) \end{cases} . \tag{2}$$

The angle θ_2 is the difference between angles φ and β, which can be expressed as

$$\theta_2 = \arccos\left(\frac{L_2^2 + a^2 + b^2 - L_1^2}{2L_2 c}\right) + \arcsin\left(\frac{b}{c}\right) - \frac{\pi}{2} . \tag{3}$$

Furthermore, the swing angle δ can be obtained by subtracting angle θ_2 from angle θ_1. In this robot design, the parameter of the frame and the magnet are determined, $D_h = 25$ mm, $D_m = 8$ mm $a = 8.5$ mm, and $b = 10$ mm. The diameter of approximately 100 mm is currently the most common design size for small jellyfish robots. Considering that the diameter of the origami-based bell D_b is larger, the diameter D_t is limit to not exceed 90 mm, thus, L_2 cannot exceed 32.5 mm. Based on these conditions, an optimization can be established as

$$\begin{aligned} \min \delta = &\arccos\left(\frac{L_2^2 + a^2 + b^2 - L_1^2}{2L_2 c}\right) + \arcsin\left(\frac{b}{c}\right) \\ &- \frac{\pi}{2} - \arcsin\left(\frac{L_1 - a}{L_2}\right) \end{aligned} , \tag{4}$$

and the constraints for the solution are

$$s.t. \begin{cases} L_1 \le L_2 \\ L_2 \le 32.5 \\ \delta < \dfrac{\pi}{2} \\ \varphi > \beta \end{cases} . \tag{5}$$

Based on this optimization model, the values of L_1 and L_2 are 24.1 mm and 32.5 mm, respectively, and the optimal swing angle δ is 28.5°. Then, all parameters required for these two origami-based structures can be further determined. First, the number of valley facets n_v and the angle θ_v (equal to θ_m) are designed as 6 and 10°, respectively. Accordingly, the radius R_s and the length of edge L_e are obtained as 28.1 mm and 4.9 mm. Then, the origami-based bell's parameters D_t, θ_{bm}, and θ_{bv} can be determined are 90 mm, 10°, and 6.3 respectively. And the value of R_b is designed as 60 mm.

D. Dynamic Analysis and Actuation Design

The key positions of designed bio-inspired jellyfish robot are shown in Fig. 2(d). Since the origami-based structures' movement below the horizontal position will trigger its bistable characteristics renders further use impossible, this paper defines this position as the threshold position. When the origami-based supporting structure is uninstalled, the distance between the stable position and the threshold position is d_s. After installation, due to the elasticity of the origami-based bell maintaining its stable state, it will pull down the supporting structure, and the two structures work together to reach a new stable position, which can be defined as the robot's self-recoverable stable position. The distance between this and threshold positions is d_0. Therefore, during the robot's motion, the required full driving distance under the electromagnetic force is $d_e = d_t - d_0$. And in the actuation

process, when the permanent magnet moves upward, it needs to overcome the downward reaction force F_r generated by the two origami structures. The closer the magnet is to the upper electromagnetic coil, the lager the value of F_r.

To analyze the motion of bio-inspired jellyfish robot and design appropriate parameters for the near-field magnetic actuation system, the dynamic model is established, as shown in (i) and (ii) of Fig. 2(e). The movement of the robot can be simplified as a spring-damping system, with the head and electromagnetic coil represented by the upper blue semicircle, while the rectangle below represents the magnet. Since the masses of two origami-based structures are extremely small compared to the overall mass of the robot, they are neglected. Additionally, because the robot does not have rigid hinges, friction between the parts during movement can also be ignored. Based on Newton's second law of motion, the dynamic model of the designed robot is

$$\begin{cases} m_1\ddot{y}_1 = F_m + F_f + F_d + F_s - G_1 + B_1 \\ m_2\ddot{y}_2 = -F_m - F_d - F_s - G_2 + B_2 \end{cases}, \quad (6)$$

where m_1, y_1, and B_1 are the combined masses of the electromagnetic coil and the head, their positions in the inertial coordinate system $X_0O_0Y_0$, as well as the buoyant force, respectively; m_2, y_2, and B_2 are mass of magnet, its position in $X_0O_0Y_0$ coordinate, and its buoyant force, respectively; F_m is the magnetic force exerted by the electromagnetic coil on the magnet; F_f, F_d, and F_s respectively represent the vertical fluid force, the fluid damping force, and the elastic force generated by the origami structures during motion.

The magnetic force can be used for determining the parameters of electromagnetic coil, it can be expressed as

$$F_m = \frac{\mu_0 n_t n_l m_x \cdot I}{2L_c\left(R_2 - R_1\right)} \cdot \left[g\left(y_2 - y_1\right) - g\left(y_2 - y_1 - L_c\right) \right]. \quad (7)$$

Where μ_0 is the vacuum permeability, n_l is the number of layers of coil; n_t is the number of turns per layer; m_x is the magnetic moment of the magnet; I is the driving current; L_c is the width of the coil, R_1 and R_2 are the minimum and maximum radii of the coil, respectively. And the function $g(\cdot)$ can be expressed as

$$g(\gamma) = \ln\frac{R_2 + \sqrt{\gamma^2 + R_2^2}}{R_1 + \sqrt{\gamma^2 + R_1^2}} + \gamma^2 \cdot \frac{\sqrt{\gamma^2 + R_1^2}\cdot\left(R_1 + \sqrt{\gamma^2 + R_1^2}\right) - \sqrt{\gamma^2 + R_2^2}\cdot\left(R_2 + \sqrt{\gamma^2 + R_2^2}\right)}{\sqrt{\gamma^2 + R_1^2}\cdot\sqrt{\gamma^2 + R_2^2}\cdot\left(R_1 + \sqrt{\gamma^2 + R_1^2}\right)\cdot\left(R_2 + \sqrt{\gamma^2 + R_2^2}\right)} \cdot \quad (8)$$

By experiment testing, the designed origami-based supporting structure's reaction force F_u is 0.285 N, and the distance d_s is 12.2 mm. When two origami-based structures are installed and reach a new stable position, their driving distance d_e is 7 mm. Furthermore, the results of reaction force F_r variation with distance obtained from underwater environment testing are shown in the Fig. 2(f), to achieve full driving distance actuation, the driving force must be greater than 1.53 N, and throughout the entire driving process, the driving force at each position must larger than the tested F_r. Based on this requirement, the parameters of near-field actuation system can be determined according to Eq. (7). Finally, under the condition of using the magnet with a length of 8 mm and the outer and inner diameter of 8 mm and 3 mm, respectively. And the minimum and maximum radii of the coil are 2.5 mm and 7 mm, respectively. The other design parameters are L_c = 5.8 mm, $n_t \cdot n_l = 200$. When I =4 A, the calculated driving force curve is shown in Fig. 2(f). After determining the parameters of actuation system. The jellyfish robot is fabricated, the diameter, height and weight of this robot are 101.6 mm, 63.8 mm, and 12.5 g, respectively.

III. Results and Discussion

A. Thrust Force and Motion Analysis

The experimental system is set up prior to performance testing. The driving signal is generated by MATLAB to control the function generator and is subsequently amplified by a power amplifier (Aigtek, ATA-308C) for the motion driving of the bio-inspired jellyfish robot. Simultaneously, an oscilloscope (Tektronix, TBS1102X) is employed to monitor the voltage waveform, ensuring signal fidelity. The thrust force is measured by a force sensor (ATI, Nano 17Ti). Meanwhile, an industrial camera is used for robot motion capture and for analyzing position and velocity. In the closed-loop control, real-time image processing algorithms are applied to the images captured by the industrial camera to obtain position and velocity information. MATLAB then sends updated control signals to the function generator based on this information, enabling real-time robot control.

In this work, a square wave signal is used to control the driving current. Since the designed robot can automatically return to its stable position under the influence of the origami-based structures, the bias ratio of the driving currents is set to 100% in all experiments to ensure efficient energy utilization. Then, under a 50% duty cycle (D_C) and 1 Hz frequency (f), the thrust and the magnet's driving distance of the robot in a fixed underwater state was tested at different driving currents. As shown in Fig. 3(a), when the driving current is I = 4 A, the magnet reaches its maximum driving distance, confirming the feasibility of the electromagnetic coil design parameters. At this moment, the instantaneous thrust generated by the robot is 0.31 N. And it can be observed that when the driving current exceeds 4 A, the thrust continues to increase, but compared to the growth trend when the driving current is less than 4 A, the slope of the increase significantly slows down. This is because the instantaneous thrust measured at a fixed state includes the lift generated by water displacement during the robot's movement and inertial forces generated by the magnet being instantaneously driven upward. When I = 4 A, the increase in driving distance caused by the rising current leads to an increase in the water displacement of the robot, thereby enhancing the lift. Once the maximum driving distance is reached, the water displacement no longer increases, and the additional thrust only results from the increased inertia force caused by the magnet experiencing a greater driving force.

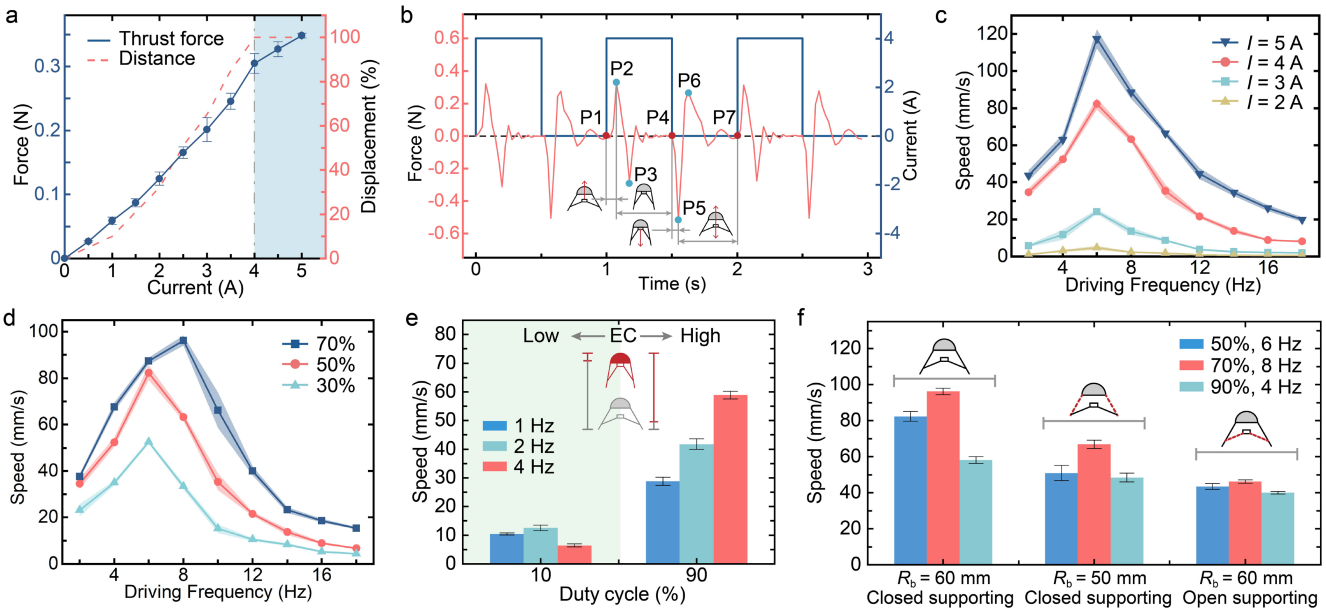

Fig. 3. The locomotion performance of the bio-inspired jellyfish robot. (a) Thrust curve and distance d_c completion rate curve versus driving current, $f = 1$ Hz. (b) Thrust curve at driving parameters $I = 4$ A, $D_C = 50\%$, $f = 1$ Hz. (c) Curves of locomotion speed versus driving frequencies under different driving currents at the duty cycle of 50%. (d) Curves of locomotion speed versus driving frequencies at duty cycles of 30%, 50%, and 70%, respectively ($I = 4$ A). (e) The locomotion speeds at different frequencies with duty cycles of 10% and 90% when $I = 4$ A. (f) Comparison of the locomotion speeds of the designed robot with closed supporting and $R_b = 60$ mm, the robot with closed supporting and $R_b = 50$ mm, and the robot with opened supporting and $R_b = 60$ mm .

Subsequently, as shown in Fig. 3(b), by analyzing the thrust curve of the robot within one driving cycle when $I = 4$ A, $D_C = 50\%$, $f = 1$ Hz, the robot's motion can be characterized, with the robot remaining in a stable position at points P1 and P7. The motion cycle between these points can be divided into four distinct stages:

Contraction stage (P1 to P2): after receiving the driving current, the robot rapidly contracts and completes the full driving distance in approximately 0.05 s at P2. And it generates the maximum instantaneous thrust of 0.31 N.

Glide stage (P2 to P4): since the driving current remains constant, the robot can maintain the contraction state, which facilitates low-resistance gliding. And after P2, under this fixed-position measurement, a counteracting value of the same magnitude as the thrust because no additional thrust is produced (P3) and then gradually stabilizing (P4).

Self-recovery stage (P4 to P5): when the driving current is discontinued (P4), the robot rapidly expansions under the reaction force F_r of the origami-based structures, reaching the maximum recovery distance in approximately 0.025 s, which results in a downward maximum force of about 0.51 N (P5).

Oscillation stage (P5 to P7): In the absence of driving current, the robot oscillates freely under the reaction force F_r until gradually returning to the stable state, and the thrust exhibits a transition from oscillation (P6) to stabilization (P7).

B. Locomotion with Different Driving Frequencies

To analyze the locomotion performance of bio-inspired jellyfish robot, under a duty cycle of 50%, the robot's locomotion speeds were tested at different driving frequencies when the driving currents are 2 A, 3 A, 4 A, and 5 A, respectively. It can be observed that under the same driving current, as the driving frequency increases, the robot's locomotion speed gradually rises (Fig. 3(c)). When the driving frequency reaches 6 Hz, the speed attains its maximum value. Beyond this point, as the frequency continues to increase, the locomotion speed gradually decreases. Take the example of $I = 4$ A, this is because, at a 50% duty cycle and a 6 Hz driving frequency, the maximum driving frequency is achieved while ensuring that each motion cycle reaches the full driving distance, thereby maximizing the driving speed and minimizing the impact of the reaction force on robot. However, when $f < 6$ Hz, the reaction force significantly reduces the locomotion speed. And when $f > 6$ Hz, each motion cycle cannot reach the full driving distance, which reduces the speed. Additionally, when $f > 6$ Hz, the robot's locomotion speed no longer shows a significant increase and remains at a relatively low value at 14 Hz. At this point, the origami-based bell and supporting structure only exhibit small-range, high-frequency vibrations, which are insufficient to generate significant water displacement, resulting in a lower speed.

Meanwhile, Fig. 3(c) clearly shows that at the same frequency, a higher driving current results in a faster robot locomotion speed, which is consistent with the thrust analysis. Under a 4 A current that achieves the full driving distance, the maximum speed at 6 Hz is 82.4 mm/s. When using a higher driving current ($I = 5$ A), a greater speed can be obtained (117.5 mm/s). Theoretically, increasing the driving current continuously can improve the speed. Based on the thrust analysis results, although the thrust continues to increase when $I > 4$ A, the energy utilization efficiency will be significantly reduced. Therefore, the robot's locomotion performance is only discussed under the 4 A driving current in the following tests.

C. Locomotion with Different Duty Cycles

As another important control parameter affecting the bio-inspired jellyfish robot's locomotion performance, the duty cycle was tested under a driving current of 4 A. The robot's locomotion speed was measured as the driving

frequency varied, with duty cycles of 10%, 30%, 50%, 70%, and 90%, respectively. Since the duty cycle represents the duration of continuous input current at the same current value, it directly determines the energy consumed by the robot's drive. Therefore, from an energy perspective, this paper categorizes the duty cycle into medium energy consumption area (D_C from 30% to 70%), low energy consumption area ($D_C < 30\%$), and high energy consumption area ($D_C > 70\%$).

As shown in Fig. 3(d), in the medium energy consumption area, a clear regularity can be observed. Under the same driving current and frequency, as the duty cycle increases, the robot's locomotion speed also increases. This is because a higher duty cycle results in the robot consuming more energy to maintain its shape after contraction, thereby extending the glide stage. Meanwhile, the oscillations caused by the reaction force of the origami-based structures are weakened, leading to a reduction in their impact on the speed. Then, at the same duty cycle, as the driving frequency increases, the robot's locomotion speed initially increases, then decreases, and finally tends to stabilize when $f > 14$ Hz. Taking the peed at D_C = 50% as a reference, when D_C = 30%, the maximum speed (52.6 mm/s) is achieved also at a driving frequency of 6 Hz. Differently, when the duty cycle is 70%, the robot under the current design parameters attains an optimal locomotion speed (96.2 mm/s) at a driving frequency of 8 Hz.

Under a 10% duty cycle, the robot's locomotion speed does not exceed 13 mm/s at different frequencies (Fig. 3(e)). This is because, when the duty cycle is low, the robot nearly has no glide stage after reaching its full driving distance, spending most of the time in oscillation stage. According to the robot's motion analysis based on thrust, under a driving current of 4 A, the contraction time required for the robot to reach full driving distance is approximately 0.05 s. Therefore, each cycle's driving time $T_D = 1/2 \times 10\% = 0.05$ s, when the driving frequency is 2 Hz, precisely matches the time needed for a single full driving distance. Compared to at a duty cycle of 1 Hz, this allows for two full driving distance cycles per second, making the driving speed fastest at 2 Hz. When the frequency exceeds 2 Hz, the driving time per cycle cannot accommodate a full driving distance, severely reducing the speed. Thus, while low duty cycles can achieve low-energy consumption driving, they limit the locomotion speed.

The optimal driving frequency at 90% duty cycle is 4 Hz, with a locomotion speed of 58.1 mm/s (Fig. 3(e)). This is because, at this duty cycle, the driving time for one driving cycle of the robot is 0.025 s, but the recovery time under driven is $T_R = 1/4 \times 10\% = 0.025$ s, precisely matching the required recovery time of the origami-based structures. When $f > 4$ Hz, the origami-based structures does not have sufficient time to recover to a stable state before being driven again, preventing the achievement of full driving distance motion for robot. Therefore, the locomotion speed under a 90% duty cycle only performs better than other duty cycles at low driving frequencies ($f \leq 2$ Hz), and its maximum locomotion speed is lower than the optimal speeds at 70% and 50% duty cycles. Therefore, in the environments where there are no restrictions on the robot's driving frequency, the preferred control parameters with 4 A driving current, 70% duty cycle and 8 Hz driving frequency should be selected to achieve the maximum locomotion speed of 96.2 mm/s.

The operation of electromagnetic coils generates heat, which has long limited the wide application of magnetic actuation systems. This design places the coil in direct contact with the surrounding liquid, which not only eliminates the need for waterproofing measures but also improves heat dissipation, thereby enhancing the robot's durability and operational stability. Additionally, since a jellyfish naturally stays in an expansion state and the magnet is positioned away from the coil, a higher driving current (4 A) is required to contract the body and maintain gliding at optimal speeds, but increasing energy consumption. To optimize energy efficiency, the robot can be modified so that the magnet and coil are in contact, allowing it to maintain a stable contraction state without continuous driving force. A lower driving current would then suffice for quick expansion movements, thereby further improving energy efficiency.

D. Performance Comparison and Motion Demonstration

To enhance the robot's locomotion speed, this design employs a closed origami-based supporting structure to increase the water displacement during each motion cycle, while also design a skirt-like structure (R_b = 60 mm) to generate auxiliary thrust during swinging. To verify the superiority of this robot structure, two robots of the same scale were fabricated: one using the same closed supporting structure with R_b = 50 mm, and another using an open structure (similar to a linkage mechanism) with R_b = 60 mm as transmission structure. Then, the locomotion of three robots was controlled at the respective optimal driving frequencies under different duty cycles: 6 Hz with 50% D_C, 8 Hz with 70% D_C, and 4 Hz with 90% D_C, all under a driving current of 4 A. Their locomotion speeds are shown in the Fig. 3(f). It can be shown that, under all three sets of driving parameters, the designed robot in this work (with closed origami-based supporting structure, R_b = 60 mm) exhibits the fastest locomotion speed in these three robots, demonstrating the superiority of the designed. Additionally, the locomotion speed of the robot with closed supporting (R_b is 50 mm) under all three sets of driving parameters is significantly higher than that of robot with open supporting (R_b = 60 mm). This indicates that, compared to traditional linkage transmission mechanisms, using the proposed closed origami-based supporting structure can effectively enhance water displacement, thereby increasing the locomotion speed of the bio-inspired jellyfish robot.

Finally, the functionality of the designed bio-inspired jellyfish robot in achieving variable-speed locomotion control to reach target positions was verified. As shown in Fig. 4, a vision-based robot position monitoring method was employed to track the robot's position and velocity in real time. During the process of locomotion from the initial position to the target object (Fig. 4(i)), the robot first swam upward under driving parameters of 1 Hz frequency, 70% duty cycle, and 4 A driving current. Once it was actuated to have moved upward 110 mm (Fig. 4(ii)), the frequency was automatically adjusted to 20 Hz to enable near-hovering motion. Subsequently, the robot rapidly swam to the target position and collided with the target under the optimal driving parameters (70% duty cycle, 8 Hz frequency, 4 A driving current) that maximize its locomotion speed, as shown in Fig.4(iii) to (v).

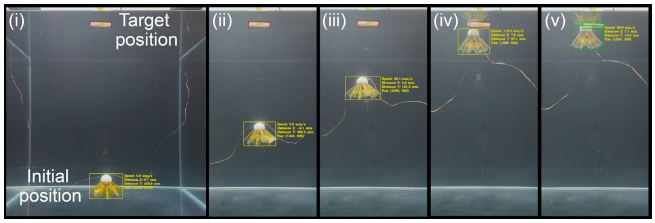

Fig. 4. Demonstration of visual-based locomotion control.

IV. Conclusion

Inspired by the unique symmetrical body structure and efficient water jet propulsion of the jellyfish, this study developed a small-scale, lightweight, and structurally compact bio-inspired jellyfish robot. The robot features a diameter of 101.6 mm, a height of 63.8 mm, and a weight of only 12.5 g. To replicate the jellyfish's locomotion, an improved waterbomb-based origami design method was proposed, along with the development of the origami-based bell and origami-based supporting structure. The integration of these components enables the robot to automatically recover to a stable state during operation, thereby conserving energy. An optimization model was established to determine the optimal design parameters of these two structures to increase water displacement per motion cycle and enhance locomotion speed. Additionally, a near-field magnetic actuation system was designed, significantly simplifying the system architecture and allowing for silent, low-friction underwater operation without waterproofing requirements. Experimental results under various driving parameters demonstrated the robot's underwater locomotion, with a maximum speed of 96.2 mm/s achieved at a driving current of 4 A, a frequency of 8 Hz, a duty cycle of 70%, and a bias current of 100%.

In future work, the steering capability of the bio-inspired jellyfish robot will be studied. A feasible solution is to introduce controlled geometric or actuation asymmetry to break reciprocity, such as through the coordinated drive of a multi-coil system arranged on a hemispherical surface to drive the permanent magnet in different directions. The magnet's motion can then be transmitted to the outer origami-based bell via the supporting structure, enabling the jellyfish robot to achieve turning control through asymmetric swinging. Additionally, using intelligent materials such as shape memory alloys to actively alter the shape of the bell at different positions is another promising scheme worth exploring. Furthermore, designing a controllable, deformable bell structure would endow the robot with multi-mode movement capabilities, which is beneficial for enhancing the motion performance of the jellyfish robot. Subsequently, system integration of the robot will be enhanced to achieve untethered operation. Finally, incorporating group control methods for the bio-inspired jellyfish robots will facilitate multi-robot underwater cooperation and control, representing an exciting area for future investigation.

References

[1] L. Chen, R. Cui, W. Yan, C. Yang, Z. Li, and H. Xu, "Stability criterion and stability enhancement for a thruster-assisted underwater hexapod robot." *IEEE Transactions on Robotics*, vol. 41, pp. 42-61, 2024.

[2] X. Liu, S. Jin, Y. Shao, S. Kuperman, A. Pratt, D. Zhang, J. Lo, Y. L. Joo, A. D. Gat, L. A. Archer, and R. F. Shepherd, "The multifunctional use of an aqueous battery for a high capacity jellyfish robot." *Science Advances*, vol. 10, no. 48, p. eadq7430, 2024.

[3] Y. Wang, P. Zhang, H. Huang, and J. Zhu, "Bio-inspired transparent soft jellyfish robot." *Soft Robotics*, vol. 10, no. 3, pp. 590-600, 2022.

[4] H. Li, S. Cui, X. Wang, B. Yu, G. Wang, C. Cao, Y. Shen, and Q. Zeng, "Development of a bionic jellyfish robot for collecting polymetallic nodules." *Ocean Engineering*, vol. 324, p. 120655, 2025.

[5] J. Sun, C. Li, M. Zhang, L. Shen, and S. Gao, "A jellyfish robot based on two-bar and four-spring tensegrity structures." *Ocean Engineering*, vol. 300, p. 117472, 2024.

[6] S. Wang, Z. Qiao, Z. Li, Y. Zhang, A. Cheng, B. Zhu, X. Yue, Y. Chen, T.-W. Wong, and G. Li, "Jellyfish-inspired soft robot driven by pneumatic bistable actuators." *Soft Robotics*, vol. 12, no. 1, pp. 1-12, 2024.

[7] Y. Chi, Y. Tang, H. Liu, and J. Yin, "Leveraging monostable and bistable pre-curved bilayer actuators for high-performance multitask soft robots." *Advanced Materials Technologies*, vol. 5, p. 2000370, 2020.

[8] R. Luo, S. Li, and F. Wang, "Design and motion characteristics analysis of underwater biomimetic jellyfish based on shape memory alloy springs." *Ocean Engineering*, vol. 297, no. 1, p. 117069, 2024.

[9] Y. Almubarak, M. Punnoose, N. X. Maly, A. Hamidi, and Y. Tadesse, "KryptoJelly: a jellyfish robot with confined, adjustable pre-stress, and easily replaceable shape memory alloy NiTi actuators." *Smart Materials and Structures*, vol. 29, no. 7, p. 075011, 2020.

[10] S. Wang and Z. Chen, "Modeling of two-dimensionally maneuverable jellyfish-inspired robot enabled by multiple soft actuators." *IEEE-ASME Transactions on Mechatronics*, vol. 27, no. 4, pp. 1998-2006, 2022.

[11] Y. Chen, H. Zhao, J. Mao, P. Chirarattananon, E. F. Helbling, N. P. Hyun, D. R. Clarke, and R. J. Wood, "Controlled flight of a microrobot powered by soft artificial muscles." *Nature*, vol. 575, pp. 324-329, 2019.

[12] T. Wang, H.-J. Joo, S. Song, W. Hu, C. Keplinger, and M. Sitti, "A versatile jellyfish-like robotic platform for effective underwater propulsion and manipulation." *Science Advances*, vol. 9, no. 15, p. eadg0292, 2023.

[13] M. Wang, T. Wu, R. Liu, Z. Zhang, J. Liu, "Selective and independent control of microrobots in a magnetic field: a review." *Engineering*, vol. 24, pp. 21-38, 2023.

[14] T. Bujard, F. Giorgio-Serchi, and G. D. Weymouth, "A resonant squid-inspired robot unlocks biological propulsive efficiency." *Science Robotics*, vol. 6, no. 50, p. eabd2971, 2021.

[15] C. Xu, Y. Cao, J. Zhao, Y. Huang, Y. Lin, D. Wang, Z. Zhang, and H. Jiang, "Muscle-inspired elasto-electromagnetic mechanism in autonomous insect robots." *Nature Communications*, vol. 16, no. 1, p. 6813, 2025.

[16] Z. Ren, W. Hu, X. Dong and M. Sitti, "Multi-functional soft-bodied jellyfish-like swimming." *Nature Communications*, vol. 10, no. 1, p. 2703, 2019.

[17] S. Wang, P. Yan, H. Huang, N. Zhang, and B. Li, "Inflatable metamorphic origami." *Research*, vol. 6, p. Artical0133, 2023.

[18] Y. Zhu and E. T. Filipov, "Large-scale modular and uniformly thick origami-inspired adaptable and load-carrying structures." *Nature Communications*, vol. 14, no. 1, p. 2353, 2024.

[19] K. Fu, X. Wu, S. Yu, Q. Zhang, Y. Yang, T. Xu, W. Yao, T. Yi, H. Li, Y. Chen, X. Zhang, and X. Chen, "Origami exoskeletons for enhanced soft robotic manipulation." *Science Advances*, vol. 11, p. eadv6629, 2025.

[20] B. H. Hanna, S. P. Magleby, R. J. Lang, and L. L. Howell, "Force-deflection modeling for generalized origami waterbomb-base mechanisms." *Journal of Applied Mechanics*, vol. 82, no. 8, p. 081001, 2015.

[21] H. Zhang, B. Zhu, B. Chen, C. Cui, H. Li, and X. Zhang, "A phase diagram-based stability design method for a symmetrical origami waterbomb base." *ASME Journal of Mechanical Design*, vol. 144, no. 10, p. 103303, 2022.

[22] D. Tang, C. Zhang, C. Pan, H. Hu, H. Sun, H. Dai, J. Fu, C. Majidi, and P. Zhao, "Bistable soft jumper capable of fast response and high takeoff velocity." *Science Robotics*, vol. 9, p. eadm8484, 2024.